Assessing Myocardial Microstructure With Biophysical Models of Diffusion MRI

Mohsen Farzi, *Member, IEEE*, Darryl McClymont, Hannah Whittington, Marie-Christine Zdora, Leah Khazin, Craig A. Lygate, Christoph Rau, Erica Dall'Armellina, Irvin Teh, and Jürgen E. Schneider

***Abstract*— Biophysical models are a promising means for interpreting diffusion weighted magnetic resonance imaging (DW-MRI) data, as they can provide estimates of physiologically relevant parameters of microstructure including cell size, volume fraction, or dispersion. However, their application in cardiac microstructure mapping (CMM) has been limited. This study proposes seven new two-compartment models with combination of restricted cylinder models and a diffusion tensor to represent intra- and extracellular spaces, respectively. Three extended versions of the cylinder model are studied here: cylinder with elliptical cross section (ECS), cylinder with Gamma distributed radii (GDR), and cylinder with Bingham distributed axes (BDA). The proposed models were applied to data in two fixed mouse hearts, acquired with multiple diffusion times, q-shells and diffusion encoding directions. The cylinderGDR-pancake model provided the best performance in terms of root mean squared error (RMSE) reducing it by 25% compared to diffusion tensor imaging (DTI). The cylinderBDA-pancake model represented anatomical findings closest as it also allows for modelling dispersion. High-resolution 3D synchrotron X-ray imaging (SRI) data from the same specimen was utilized to evaluate the biophysical models. A novel tensor-based registration method is proposed to align SRI structure tensors to the MR diffusion tensors. The consistency between SRI and DW-MRI parameters demonstrates the potential of compartment models in assessing physiologically relevant parameters.**

***Index Terms*— Cardiac microstructure mapping (CMM), biophysical models, compartment modelling, diffusion weighted MRI, synchrotron X-ray imaging.**

I. Introduction

THE heart is composed of cardiomyocytes, fibroblasts, vessels, and nerves surrounded by a supporting collagen matrix. Cardiomyocytes are organised into laminar planes known as sheetlets separated by small cleft-like spaces (Fig. 1) [1]. Within each sheetlet, cardiomyocytes are locally-aligned where the cardiomyocyte orientation is defined in the direction of their long axes. The cardiomyocyte direction varies transmurally from a left-handed helix at the subepicardium to right-handed helix at subendocardium. This helical microstructure has a fundamental influence on the electro-mechanical functionality of the heart [1]–[3]. Dysregulation of this structure is a key determinant of heart failure [4]–[6]. This central role of myocardial microstructure has motivated the development of non-invasive imaging techniques to visualise and quantify cardiac micro-architectural properties known as cardiac microstructure mapping (CMM).

Diffusion weighted Magnetic Resonance Imaging (DW-MRI) is a valuable non-invasive method for probing complex structures in biological tissues [7], [8]. DW-MRI reconstruction can be broadly divided in two categories [9], [10]: *signal representations* and *biophysical models*. Diffusion tensor imaging (DTI) is the most commonly used technique in the first category [7], [11]. In DTI, the principal eigenvectors reflect the orientation of cardiomyocytes and sheetlets, and macroscopic diffusion metrics indicate the underlying tissue integrity. DTI parameters, despite being sensitive to the underlying microstructure, remain an indirect characterisation of tissue-specific properties such as cardiomyocyte diameter and volume fraction.

The ability to map cellular-level biophysical parameters has the potential to significantly benefit clinical applications [14]. This objective cannot be achieved using signal

Manuscript received May 20, 2021; revised July 4, 2021; accepted July 9, 2021. Date of publication July 16, 2021; date of current version November 30, 2021. This work was supported in part by the British Heart Foundation (BHF) under Grant PG/17/28/32943, Grant PG/19/1/34076, and Grant RG/13/8/30266; and in part by the Diamond Light Source, Instrument I13-2 through Synchrotron X-Ray Imaging (SRI) Experiments under Grant MT15287. *(Corresponding author: Jürgen E. Schneider.)*

This work involved animals in its research. Approval of all ethical and experimental protocols was obtained from the Committee for Animal Care and Ethical Review at the University of Oxford and granted by the U.K. Home Office under Project License No. 30-3314, and performed in line with the Animals (Scientific Procedures) Act of 1986 and Directive 2010/63/EU of the European Parliament.

Mohsen Farzi, Leah Khazin, Erica Dall'Armellina, Irvin Teh, and Jürgen E. Schneider are with the Department of Biomedical Imagining Science, Cardiovascular and Metabolic Medicine, University of Leeds, Leeds LS2 9JT, U.K. (e-mail: m.farzi@leeds.ac.uk; l.khazin@leeds.ac.uk; e.dallarmellina@leeds.ac.uk; i.teh@leeds.ac.uk; j.e.schneider@leeds.ac.uk).

Darryl McClymont and Hannah Whittington were with the Division of Cardiovascular Medicine, University of Oxford, Oxford OX3 9DU, U.K. (e-mail: darryl.mcclymont@gmail.com; h.whittington228@gmail.com).

Marie-Christine Zdora was with the Department of Physics and Astronomy, University College London, London WC1E 6BT, U.K., and also with Diamond Light Source Ltd., Didcot, Oxfordshire OX11 0DE, U.K. She is now with the Paul Scherrer Institute, 5232 Villigen, Switzerland (e-mail: marie.zdora@psi.ch).

Craig A. Lygate is with the Division of Cardiovascular Medicine, University of Oxford, Oxford OX3 9DU, U.K. (e-mail: clygate@well.ox.ac.uk).

Christoph Rau is with Diamond Light Source Ltd., Didcot, Oxfordshire OX11 0DE, U.K. (e-mail: christoph.rau@diamond.ac.uk).

This article has supplementary downloadable material available at https://doi.org/10.1109/TMI.2021.3097907, provided by the authors.

Digital Object Identifier 10.1109/TMI.2021.3097907

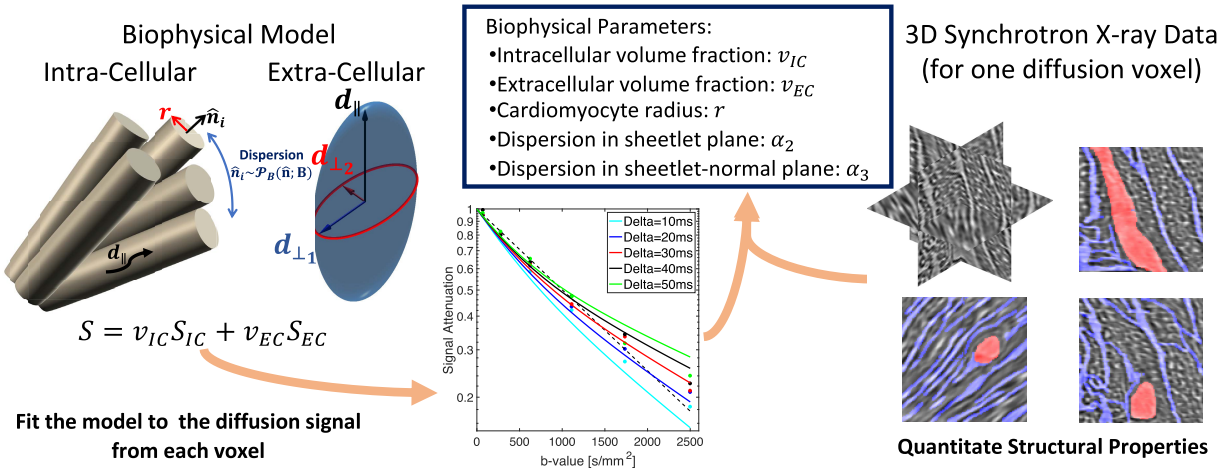

Fig. 1. Proposed CMM Pipeline. Diffusion signal from each voxel is modelled as a linear combination of signals from two compartments representing the intra- and extracellular space, respectively. To model signal from aggregation of cardiomyocytes in each voxel, the standard cylinder model [12] was extended such that each cylinder axis is drawn from a Bingham distribution [13]. Hindered diffusion from the extracellular space is modelled with a single diffusion tensor. Estimated biophysical parameters are then validated against information from SRI data that provides ≈ 85 times better spatial resolution with respect to the DW-MRI. Vessels and the extracellular space are coloured in red and blue, respectively.

representation techniques including DTI, diffusion kurtosis imaging (DKI) [6], or diffusion spectrum imaging (DSI) [15], [16]. Biophysical models, on the other hand, can potentially provide direct estimations of specific tissue features such as cell orientation, dispersion, diameter, and volume, which are of physiological/biomedical relevance. In this approach, the underlying tissue environment is represented by a combination of basic geometrical compartments with known analytic expressions for diffusion signals. The model parameters are then estimated by comparing the empirical signal measurements against those predicted from the model [14].

Biophysical models are increasingly used in the brain [10], [17], [18]. However, their application to cardiac MRI has been scant. Hsu *et al.* [19] proposed a two-compartment model to account for non-mono-exponential diffusion signal decay at high b-values. The first component with fast diffusion was attributed to the capillary network or interstitial space, and the second component with slow diffusion was associated with the intracellular space. In another study, Kim *et al.* [12] proposed a two-compartment model where the intra- and extracellular space were represented by impermeable cylinders and unrestricted isotropic tensors, respectively.

Despite the merits of these models, they have failed to yield realistic parameters in agreement with reported physiological ranges [20], [21] or fit the diffusion signal sufficiently well. Previous studies were also restricted in the DW acquisition scheme. In [12], the gradient strength was fixed and data were collected at different diffusion times. Conversely, in [19], the diffusion time was fixed and data were collected at different b-values. In brain microstructure mapping, it has been shown that estimating cell sizes and shapes requires diffusion information with multiple q-shells and diffusion times [22].

To address these limitations, this paper focuses on three aspects. First, a range of novel biophysical models tailored to cardiac applications were developed and evaluated in the preclinical setting to quantify cardiomyocyte size, orientation, dispersion, and volume fraction. The contribution of the total DW-MRI signal is modelled by two separate non-exchanging compartments attributed to water molecules inside the cardiomyocytes and the interstitial space between them. This framework is built on our previous work where a cylinder model with elliptical cross section (ECS) was introduced to model intracellular diffusion signal from cardiomyocytes [23]. Here two more extended versions of the standard cylinder model are studied: cylinder with Gamma distributed radii (GDR) and cylinder with Bingham distributed axes (BDA). The models are compared against each other to identify which one captures the diffusion signal best and, at the same time, provides a plausible and accurate estimation of desired biophysical parameters. Second, to facilitate parameter estimation for biophysical models, new acquisition schemes were investigated that collect multi-diffusion-time, multi-shell, and multi-direction data. We show that previous acquisitions schemes that only acquired a single shell with different diffusion times, or multiple shells but with a single diffusion time are insufficient. Third, synchrotron X-ray imaging (SRI) was used to provide independent gold-standard measurements of the tissue microstructure at a spatial resolution far higher than available in MRI (section II-B; [24]).

II. Methods

Fig. 1 shows the proposed framework for CMM. Section II-A describes the biophysical models. In section II-B, microstructure parameter estimation using the SRI dataset is demonstrated. Finally, section II-C describes the sample acquisition protocols for both MRI and SRI.

A. Theory

The total normalised MR signal S is modelled as a linear combination of signals from the intracellular (IC) and extracellular (EC) space:

$$S = v_{\mathrm{IC}} S_{\mathrm{IC}} + v_{\mathrm{EC}} S_{\mathrm{EC}}, \quad (1)$$

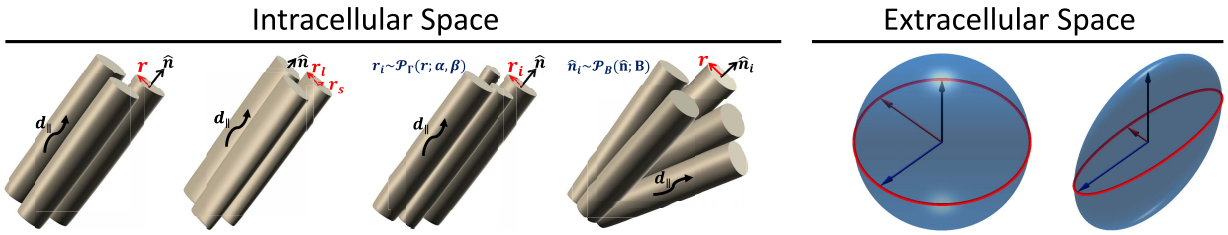

Fig. 2. Intracellular and Extracellular Compartments. To model restricted diffusion inside cardiomyocytes, four cylinder models were utilised. From left to right, the standard model [12], cylinders with ECS [23], cylinders with GDR [25], and cylinders with BDA are shown, respectively. To model hindered diffusion in the extracellular space, an isotropic tensor (ball) with $d_1 = d_2 = d_3$ and an oblate tensor (pancake) with $d_1 = d_2 \geq d_3$ were utilised, where d_1, d_2, and d_3 are the primary, secondary, and tertiary diffusion eigenvalues.

where $\{v_{\text{IC}}, v_{\text{EC}}\} \in [0, 1]$ are volume fractions for each compartment and $v_{\text{IC}} + v_{\text{EC}} = 1$. Here, the interstitial space and vascular components are lumped into one effective compartment similar to Hsu *et al.* [19], Kim *et al.* [12].

Hindered diffusion of water molecules in the extracellular space is modelled using a symmetric diffusion tensor $\mathbf{D}$. The normalised signal is

$$S_{\text{EC}} = \exp[-b\,\hat{\boldsymbol{g}}\,\mathbf{D}\,\hat{\boldsymbol{g}}], \tag{2}$$

where $b = \gamma^2\delta^2(\Delta - \delta/3)|\boldsymbol{g}|^2$ for the PGSE sequence, Δ is the diffusion time, δ is the diffusion gradient duration, γ is the gyromagnetic ratio, and $|\boldsymbol{g}|$ and $\hat{\boldsymbol{g}}$ are the gradient magnitude and direction, respectively. Two different tensor models with isotropic diffusivity (ball) and oblate anisotropy (pancake) were studied here. (Fig. 2).

To model restricted diffusion in cardiomyocytes, four cylinder models were investigated: the standard cylinder [12], cylinder-ECS [23], cylinder-GDR [25], and cylinder-BDA (Fig. 2).

The signal model for the standard cylinder S_{cyl} is presented in Appendix A (Eq. 21). Similarly for the cylinder-ECS, the signal model is represented by the product of signals parallel to the cylinder axis $\hat{\boldsymbol{u}}_1$ and perpendicular to it along the second ($\hat{\boldsymbol{u}}_2$) and third ($\hat{\boldsymbol{u}}_3$) diffusion eigenvectors:

$$\begin{aligned} S_{\text{cyl-ECS}} = s_0 &\exp -L_{\parallel}(d_{\parallel})\left[\boldsymbol{g}^T\hat{\boldsymbol{u}}_1\right]^2 \\ &\times \exp -L_{\perp}(r_l, d_{\parallel})\left[\boldsymbol{g}^T\hat{\boldsymbol{u}}_2\right]^2 \\ &\times \exp -L_{\perp}(r_s, d_{\parallel})\left[\boldsymbol{g}^T\hat{\boldsymbol{u}}_3\right]^2, \end{aligned} \tag{3}$$

where s_0 is the signal at b-value equals zero, $d_{\parallel}$ is the diffusivity along the cylinder axis $\hat{\boldsymbol{u}}_1$, and r_l and r_s are the major and minor radii along $\hat{\boldsymbol{u}}_2$ and $\hat{\boldsymbol{u}}_3$, respectively. The functions $L_{\parallel}$ (Eq. 22) and $L_{\perp}$ (Eq. 23) are defined in Appendix A.

Instead of a fixed cylinder radius r in the cylinder-GDR model, each r is drawn from a Gamma distribution Γ [25].

$$\mathcal{P}_{\Gamma}(r; \kappa, \nu) = \frac{r^{\kappa-1}\exp[-r/\nu]}{\Gamma(\kappa)\nu^{\kappa}}, \tag{4}$$

where $\kappa > 0$ is the shape parameter, and $\nu > 0$ is the scale parameter. The signal from the cardiomyocytes with GDR is then computed as the signal from a cylinder weighted by the Gamma distribution function:

$$S_{\text{cyl-GDR}} = s_0 \int_{r=0}^{\infty} \mathcal{P}_{\Gamma}(r; \kappa, \nu) S_{\text{cyl}}(r; \hat{\boldsymbol{n}}, d_{\parallel}) dr. \tag{5}$$

Given a typical voxel size of $\sim$ 200 µm in our DW-MRI, each voxel may include a few hundreds of myocytes. While these myocytes are locally aligned within sheetlets, they demonstrated non-linear undulation in the corresponding SRI data (supplementary Figure 1). Given micro-structure tensors within each corresponding MRI voxel, a distribution of the preferred directions along the tertiary eigenvectors can be estimated using a Bingham distribution. To model this dispersion, a new cylinder model with BDA is proposed here. Use of sticks (cylinders with $r = 0$) with BDA has previously been investigated in neuro-microstructure mapping [26], [27]. Here, the idea is generalised for cylinders with $r > 0$.

The probability density of an orientation about the mean cylinder axes $\hat{\boldsymbol{n}}$ is modelled by a Bingham distribution [13] in terms of a symmetric 3×3 matrix $\mathbf{B}$,

$$\mathcal{P}_B(\hat{\boldsymbol{n}}; \mathbf{B}) = {}_1F_1(\frac{1}{2}, \frac{3}{2}, \mathbf{B})^{-1} \exp(\hat{\boldsymbol{n}}^T\mathbf{B}\hat{\boldsymbol{n}}), \tag{6}$$

where the normalising constant ${}_1F_1(.)$ is the hypergeometric function of the first kind with a matrix argument defined as

$${}_1F_1(\frac{1}{2}, \frac{3}{2}, \mathbf{B}) = \int_{\mathbb{S}^2} \exp(\hat{\boldsymbol{n}}^T\mathbf{B}\hat{\boldsymbol{n}}) d\hat{\boldsymbol{n}}. \tag{7}$$

Note that the integration is over the unit sphere surface denoted by $\mathbb{S}^2 := \{(x, y, z) : x^2 + y^2 + z^2 = 1\}$ in the standard Cartesian space.

This extension enables quantification of cell dispersion (Fig. 3). The signal from the cardiomyocytes is then computed as the signal from a cylinder weighted by the Bingham orientation distribution function:

$$S_{\text{cyl-BDA}} = \int_{\mathbb{S}^2} \mathcal{P}_B(\hat{\boldsymbol{n}}; \mathbf{B}) S_{\text{cyl}}(\hat{\boldsymbol{n}}; d_{\parallel}, r) d\hat{\boldsymbol{n}}. \tag{8}$$

The symmetric parameter matrix $\mathbf{B}$ can be represented in the diagonalised form

$$\mathbf{B} = \left[\hat{\boldsymbol{u}}_1\ \hat{\boldsymbol{u}}_2\ \hat{\boldsymbol{u}}_3\right] \begin{bmatrix} \kappa_1 & 0 & 0 \\ 0 & \kappa_2 & 0 \\ 0 & 0 & \kappa_3 \end{bmatrix} \left[\hat{\boldsymbol{u}}_1\ \hat{\boldsymbol{u}}_2\ \hat{\boldsymbol{u}}_3\right]^T, \tag{9}$$

where $\mathbf{U} = \left[\hat{\boldsymbol{u}}_1\ \hat{\boldsymbol{u}}_2\ \hat{\boldsymbol{u}}_3\right]$ is an orthonormal frame, and κ_1, κ_2, and κ_3 are shape parameters. Note that the Bingham distribution has a degeneracy in specification of shape

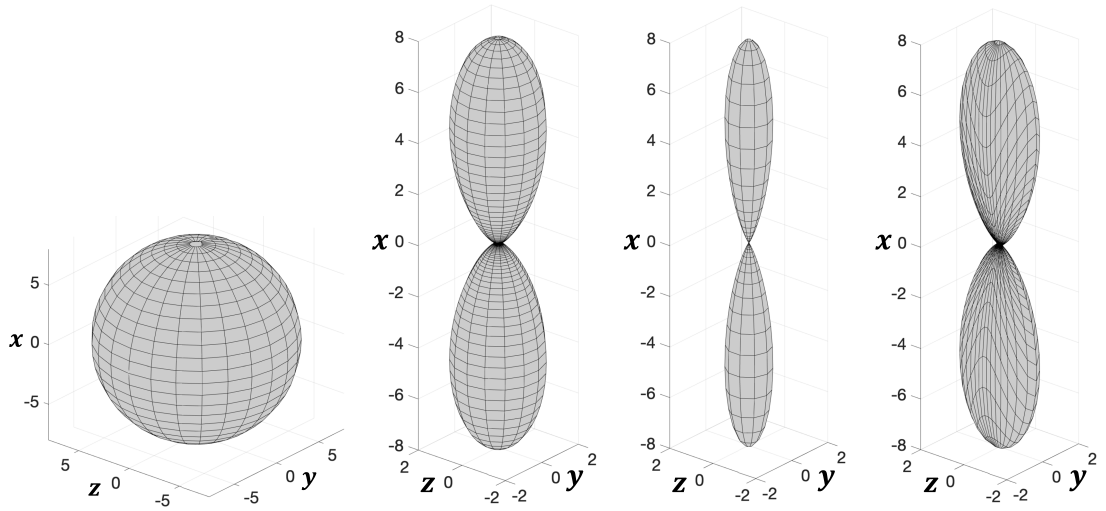

(a) $\kappa_2 = \kappa_3 = 0$ (b) $\kappa_2 = \kappa_3 = 4$ (c) $\kappa_2 = \kappa_3 = 16$ (d) $\kappa_2 = 16$ and $\kappa_3 = 4$

Fig. 3. Illustration of a set of Bingham distributions with the same orthonormal frame $U = I_{3\times3}$ and different concentration parameters $\kappa_1 = 0$, κ_2, and κ_3. For each point $p = [x,y,z]^T$ on the surface of the graphs, the distance from the centre, i.e., $\|p\|_{\ell_2} = \sqrt{x^2 + y^2 + z^2}$, represents the probability of observing a direction along $\hat{p} = p/\|p\|_{\ell_2}$, i.e., $c\mathcal{P}_B(\hat{p}; B)$, where the constant c is selected such that the maximum distance is set to eight in all plots for ease of visual demonstration. Note that the larger the distance is from the centre, the higher is the probability along that direction. (a) When $\kappa_1 = \kappa_2 = \kappa_3 = 0$, all directions are equally probable to be selected from the Bingham distribution. (b) For positive values $\kappa_2 = \kappa_3 = 4$, directions concentrated around $\hat{\boldsymbol{u}}_1 = \hat{x}$ are more likely to be selected. When $\kappa_2 = \kappa_3$, the distribution is cylindrically symmetric and reduces to a Watson distribution. (c) Increasing $\kappa_2 = \kappa_3 = 16$ decreases the dispersion around $\hat{\boldsymbol{u}}_1$. (d) When $\kappa_2 \neq \kappa_3$, dispersion around $\hat{u}_1$ is no longer isotropic.

parameters κ [13]. To address this degeneracy, we assume $\kappa_1 = 0$. Parameters κ_2 and κ_3 control the degree of dispersion around $\hat{\boldsymbol{u}}_1$. The larger the κ, the more concentrated the distribution is. Note that $\kappa_2 = \kappa_3$ models an isotropic dispersion around the axis $\hat{\boldsymbol{u}}_1$ which is equivalent to a Watson distribution (Fig. 3). For anisotropic dispersion ($\kappa_2 \neq \kappa_3$), we further assume that $\kappa_3 \geq \kappa_2$ to make sure the diffusivity along $\hat{\boldsymbol{u}}_3$ is smaller or equal to the diffusivity along $\hat{\boldsymbol{u}}_2$.

Estimating κ_2 and κ_3, the angular dispersion about the primary axis in the sheetlet plane, i.e. the plane perpendicular to $\hat{\boldsymbol{u}}_3$, and sheetlet-normal plane, i.e. the plane perpendicular to $\hat{\boldsymbol{u}}_2$, are computed as

$$\alpha_2 = \tan^{-1}(1/\kappa_2), \tag{10}$$
$$\alpha_3 = \tan^{-1}(1/\kappa_3). \tag{11}$$

1) Tissue Models: Each tissue model is named after its constituent compartments. For example, *Cylinder-Ball* is a two-compartment model where the intracellular space is modelled using the standard cylinder and the extracellular space is modelled with a ball. In total, eight different two-compartment models can be constructed by combining each of the four cylinder models with either a ball or a pancake, out of which seven models are new while one has previously been proposed by Kim *et al.* [12] (Fig. 2). Including two models previously proposed by Hsu *et al.* [19] and McClymont *et al.* [23], ten different compartment models were investigated (Table II).

In all tissue models, the primary cylinder axis is enforced to be parallel with the primary diffusion eigenvector. The intracellular diffusivity d_{IC} along the cylinder axis is constrained between 0.5 and 1.8$\mu m^2/ms$ [28]. The extracellular diffusivity d_{EC} along the primary diffusion eigenvector is constrained between 2.0 and 3.0$\mu m^2/ms$ [28]. The cylinder radius was constrained between 1 and 20 μm [20].

2) Model Fitting: To estimate the model parameters, the model is fitted to data by minimising the following cost function:

$$\mathcal{J} = \sum_{m=1}^{M} \left[\tilde{S}_m(\delta, \Delta, \boldsymbol{g}) - S_m(\delta, \Delta, \boldsymbol{g}, \boldsymbol{p})\right]^2, \tag{12}$$

where M is the total number of measurements, $\tilde{S}_m$ is the m^{th} measurement, S_m is the corresponding predicted signal from the model (Eq. 1), and vector $\boldsymbol{p}$ includes the free parameters for each tissue model.

To enforce constraints on model parameters, the method of substitution is applied similar to [25]. In this method, each constrained variable is substituted with an appropriate transformation of a corresponding unconstrained variable into the objective function to create an unconstrained composite cost function. A Levenberg-Marquardt algorithm was employed to solve the unconstrained non-linear optimisation problem. All experiments were conducted using an in-house Matlab toolkit developed for compartment modelling.

B. Biophysical Parameter Estimation Using SRI

SRI data were acquired with effective pixel size of 1.1 μm and then downsampled with a factor of two giving effective pixel size of 2.2 μm. First, the 3D structure of the samples were reconstructed from the acquired projections. Second, structure tenors were computed using quadrature filters. Third, SRI reconstructed scans were rigidly registered with DW-MRI scans such that structure tensors were aligned with diffusion tensors. Finally, biophysical parameters were quantified and

then averaged over the SRI domain corresponding to each DW-MRI voxel. Here, cardiomyocyte orientation and volume fractions were quantified using structure tensors and manual segmentation masks, respectively.

1) Image Reconstruction: SRI can provide 3D information on the inner microstructure of a sample when performed in tomographic mode. For tomographic SRI, 2D projections are acquired at different viewing angles of a rotating sample and combined together with a tomographic reconstruction algorithm to obtain a 3D volume. As a first step, the 2D projections P were corrected for the detector dark current (dark correction, $\overline{D}$) and the empty-beam profile without the sample in the beam (flat-field correction, $\overline{F}$):

$$P_c = \frac{P_r - \overline{D}}{\overline{F} - \overline{D}}, \tag{13}$$

where P_c and P_r are calibrated and raw projection data, respectively. Next, the data was rearranged into 2D sinograms by grouping the signal for each row of the projection data across all different rotation angles. Second, the centre of rotation was corrected by a translation of 20 pixels to the right along the x-axis [29]. Third, Raven filter $H_r(u, v)$ [30] was applied to remove ring artefacts [31]. Raven filter is a horizontal notch filter to reject vertical lines from the sinogram:

$$H(u, v) = \begin{cases} \dfrac{1}{1 + (\frac{u}{u_0})^{2n}} & \text{if } |v| \leq v_0 \\ 1 & \text{otherwise} \end{cases} \tag{14}$$

where u and v are the spatial frequencies. The parameters were set as $u_0 = 30$, $v_0 = 2$, and $n = 4$. Fourth, to enhance soft-tissue contrast, each 2D sinogram was smoothed with a Gaussian filter with $\sigma = 1.5$ and then passed through a logarithmic function $f(x) = 1000 \log(x)$. Finally, a filtered back-projection algorithm [32] was applied to reconstruct the 3D volume from the sinograms. All parameters were heuristically set by visual optimisation of image sharpness and contrast.

2) Structure Tensor Analysis: Structure tensors (STs) were computed based on grey level intensity gradients in the reconstructed SRI scans using the method of *quadrature filters* [24], [33], [34]. A quadrature filter with an orientation vector $\hat{\boldsymbol{n}}_k$, bandwidth B, and centre frequency f_c can be defined in the Fourier domain as:

$$\mathbf{F}_k(\boldsymbol{u}) = \begin{cases} e^{\frac{-4}{B^2 \log 2} \log(\|\boldsymbol{u}\|_2 / f_c)} \dfrac{(\boldsymbol{u}^T \hat{\boldsymbol{n}}_k)^2}{\|\boldsymbol{u}\|_2^2} & \text{if } \boldsymbol{u}^T \hat{\boldsymbol{n}}_k > 0, \\ 0 & \text{otherwise.} \end{cases} \tag{15}$$

For quadrature filters to be invariant to the rotation of axes, the orientation of each filter should be uniformly distributed on a diametrically symmetric regular polyhedron [33], [34]. Following filtering the reconstructed SRI image with quadrature filters $\mathbf{F}_k$, the filtered images q_k are used to compute the structure tensor $\mathbf{T}$ as

$$\mathbf{T} = \sum_{k=1}^{6} q_k \left[\frac{5}{4} \hat{\boldsymbol{n}}_k \hat{\boldsymbol{n}}_k^T - \frac{1}{4} \mathbf{I}_{3\times 3} \right], \tag{16}$$

where $\mathbf{I}$ is the identity tensor.

The quadrature filtering was performed in the spatial domain using freely available Matlab code [35]. Note that the role of f_c is analogous to the diffusion time (Δ) in DW-MRI; both parameters influence the size of local environment that contributes to the structure tensor/diffusion tensor. In DW-MRI, diffusion time is proportional to the root mean squared displacement of water molecules in tissues, whereas in SRI, the centre frequency should be chosen relative to the structure size of interest.

3) Image Registration: Unlike 2D histological methods that are destructive and prone to distortions, SRI analysis can be performed on the same samples prepared for MRI acquisition without further changes. Since samples are embedded in tubes filled with agarose gel, distortion artefacts are minimal, and a rigid transform is sufficient to map SRI data to the DW-MRI scans. However, finding the optimal transform is still challenging for two reasons. Firstly, grey level values in SRI data are not directly proportional to intensity values measured in DW-MRI. Secondly, a single voxel in DW-MRI represents a volume of $\approx 187^3$ voxels in SRI. Therefore, mesh-based methods with binary masks have limited accuracy (Fig. 5).

To address these challenges, a new registration method based on aligning tensor fields is proposed as follows. First, to account for the difference in voxel width w between MRI and SRI scans, the structure tensor $\mathbf{S}$ is smoothed with a 3D Gaussian filter with $\sigma = \frac{1}{2} \frac{w_{\text{mri}}}{w_{\text{sri}}}$. Next, given an estimate of the rotation matrix $\mathbf{R}$ and the translation vector $\boldsymbol{t}$, the structure tensor $\mathbf{S}$ is warped to the MRI domain in two steps. Firstly, each structure tensor element s_{ij} is transformed using a linear interpolation.

$$s'_{ij}(\boldsymbol{x}) = s_{ij}(\mathbf{R}\boldsymbol{x} + \boldsymbol{t}), \tag{17}$$

where $\boldsymbol{x}$ represent the coordinates in the DW-MRI domain. Secondly, the full element-wise warped tensor $\mathbf{S}'$ is rotated to account for the rotation of the frame.

$$\mathbf{S}'' = \mathbf{R}\mathbf{S}'. \tag{18}$$

Given the warped structure tensor $\mathbf{S}''$ and diffusion tensor $\mathbf{D}$, the cost function $\mathcal{J}_{reg}$ is computed as

$$\mathcal{J}_{reg} = 1 - \frac{1}{3|\Omega|} \sum_{i=1}^{3} \sum_{\boldsymbol{x} \in \Omega} |\boldsymbol{u}_i^T(\boldsymbol{x}) \boldsymbol{v}_{(i)}(\boldsymbol{x})|, \tag{19}$$

where $\boldsymbol{u}_i$ are the eigenvectors of diffusion tensor $\mathbf{D}$, $\boldsymbol{v}_{(i)}$ are the corresponding eigenvectors of the warped structure tensor $\mathbf{S}''$, and Ω is the selected ROI on the MRI frame over which the cost function is calculated. It has been shown in [24] that the primary, secondary, and tertiary diffusion eigenvectors correspond to the tertiary, secondary, and primary structure tensor eigenvectors, respectively. Note that $\mathcal{J}_{reg}$ is between zero and one where zero means a perfect registration. A gradient descent technique is used to minimise $\mathcal{J}_{reg}$ with respect to the rotation matrix $\mathbf{R}$ and translation vector $\boldsymbol{t}$.

4) Segmentation: A stack of $1002 \times 1002 \times 150$ voxels from the reconstructed SRI images were segmented manually into three clusters including vessels, cardiomyocytes, and the extracellular space using ITK-SNAP [36]. Based on the manual annotations, the grey-value intensity profiles for each cluster

were estimated by a Gaussian distribution. A Gaussian mixture model is then fitted to the SRI data at each corresponding DW-MRI voxel. Estimated weights for each cluster yield the volume fraction for each compartment.

To quantitate cell geometry, eight individual cardiomyocytes were manually segmented from the mid-ventricle wall (supplementary Figure 2). The mean and standard deviation (SD) for cell radius were reported in Table II.

C. Data Acquisition

1) Sample Preparation: Sample preparation was performed as described previously [28]. In brief, two hearts were excised from healthy mice, and perfused in constant pressure Langendorff mode at 80 mmHg with modified Krebs-Henseleit solution and cardioplegically arrested with STH-2 buffer. The hearts were then perfused via an aortic cannula at constant flow with 4% paraformaldehyde (PFA) and subsequently with 1% PFA. The hearts were immersed in 1% PFA and stored at 4 °C to continue fixation. Prior to imaging, the hearts were rinsed of fixative via immersion in phosphate-buffered saline (PBS) and perfusion of PBS by aortic cannula. The hearts were then embedded in 2% agarose-PBS gel (Web Scientific, Crewe, UK) to minimise sample motion for MRI and subsequent synchrotron imaging. All experimental investigations conformed to the UK Home Office guidance on the Operations of Animals (Scientific Procedures) Act 1986 and were approved by the University of Oxford ethical review board.

2) Diffusion-Weighted MR Imaging: MRI was performed on a 9.4 T preclinical MR scanner (Agilent, CA, USA) with shielded gradients (max gradient strength = 1T/m, rise time = 130 µs) and a quadrature-driven birdcage coil (Rapid Biomedical, Rimpar, Germany) of inner diameter = 20 mm. Images were acquired using a DW fast spin echo sequence with six gradient strengths and five diffusion times ($\Delta = 10, \ldots, 50$ ms), and ten diffusion-encoding directions. One non-DW image was also acquired for each diffusion time, bringing the total number of images to 305. Imaging parameters: resolution = 187.5 µm isotropic, field-of-view = $9 \times 9 \times 5$ mm, echo train length = 8, echo spacing = 3.4 ms, diffusion gradient duration $\delta = 2.5$ ms, and maximum b-value = 2500s/mm^2. The total acquisition time for MR imaging was 37 h for each mouse heart.

To improve the signal-to-noise ratio (SNR), dynamic receiver gain adjustment was used [28], and a lowpass Butterworth filter of order $n = 4$ with normalised cutoff frequency of 1/3 was applied. Similar to [12], different echo times (TE) were used for each diffusion time. To compensate for this variable TE, diffusion signals were normalised to the corresponding s_0, i.e. signal measured at $b = 0$, for each diffusion time. To segment cardiac tissue, the image collected with $\Delta = 10$ ms was used. Two features including apparent diffusion coefficient (ADC) and s_0 were extracted for each voxel. K-means clustering was used to automatically segment the cardiac tissue. Using morphological operations, small regions with less than 500 voxels were excluded.

3) Synchrotron X-Ray Imaging: SRI data were acquired at beamline I13-2 imaging branch of the Diamond Light Source (Didcot, UK) [37]. In-line phase-contrast imaging and tomography were performed using monochromatic X-rays (20-30 keV). For each full heart, a single region-of-interest (ROI) in the apical LV myocardium was imaged with an effective isotropic pixel size of 1.1 µm. We acquired 2401 projection scans (exposure time of ≈ 1.2 s) with uniform angular spacing over 180 degrees of sample rotation. To correct for the detector dark current, twenty projections were collected when the X-ray beam was blocked. For flat-field correction, twenty projections were collected without the sample in the beam. The total acquisition time was 1 h 25min. See our previous work for more details [24].

III. Experiments and Results

A. Comparison Between Biophysical Models

1) Quality of Fit: For quantitative evaluation, the average Akaike information criterion (AIC) is reported in Table II. AIC rewards models that minimise the root mean squared error (RMSE) but also penalises for an increase in the number of free parameters.

$$\mathrm{AIC} = 2n - 2\ln(\hat{L}), \tag{20}$$

where $\hat{L}$ is the maximum value of the likelihood function for the model and n is the number of estimated model parameters. Note that a lower value (signed) of AIC suggests a better model.

To reflect the overall fitting performance across the myocardium, the distribution of RMSE in one cross-section in the short-axis orientation are visualised using heat-maps (supplementary Figure 3). An overall reduction of 16.0%, 18.9%, 30.6%, and 16.6% in RMSE compared to a single diffusion tensor was observed for cylinder-pancake, cylinderECS-pancake, cylinderGDR-pancake, and cylinderBDA-pancake models, respectively (box plot in supplementary Figure 3). To assess the variation of signal residuals along all diffusion directions, Bland-Altman plots are presented in supplementary Figure 4. Unlike DTI, all presented models were unbiased estimators for the collected DW-MR signals. Fitting performance varied between different diffusion directions. Supplementary Figure 5 shows the measured DW-MRI signal and the synthesised signal from the proposed biophysical models in a single voxel along the primary, secondary, and tertiary diffusion eigenvectors. Results are only presented for the proposed models with enhanced fitting performance compared to DTI.

2) Sheetlet and Cardiomyocyte Orientation: The orientations of diffusion eigenvectors are known to reflect the spatial arrangement of the cardiac microstructure. The primary, secondary and tertiary eigenvectors correspond to the long axes of cardiomyocytes, the sheetlet and the sheetlet-normal directions, respectively. To compare the angular variability along each direction between the proposed biophysical models, the *coupled angles* $\theta_{ij} = \arctan(\boldsymbol{v}_i.\boldsymbol{u}_j)/(\boldsymbol{v}_i.\boldsymbol{u}_i)$ were computed where $\boldsymbol{u}_i$ is the i^{th} DTI eigenvector and $\boldsymbol{v}_i$ is the i^{th} principal diffusion direction estimated from the biophysical models (Fig. 4). Table I shows the average and standard deviation of each coupled angles. The average values demonstrate a

TABLE I
AVERAGE (STD) OF COUPLED ANGLES ABOUT DTI EIGENVECTORS [DEGREE]

	θ_{12}	θ_{13}	θ_{21}	θ_{23}	θ_{31}	θ_{32}
tensor-tensor [19]	0.0 (0.1)	-0.0 (0.1)	-0.0 (0.1)	-0.0 (0.2)	0.0 (0.1)	0.0 (0.2)
cylinder-ball [12]	-1.2 (1.9)	-0.2 (1.0)	-0.7 (8.5)	-6.3 (65.4)	0.5 (10.2)	6.3 (65.4)
cylinderECS-ball-stick [23]	0.1 (2.3)	0.1 (0.8)	-0.1 (2.3)	0.3 (1.8)	-0.1 (0.8)	-0.3 (1.8)
cylinderECS-ball	0.0 (0.6)	0.1 (0.4)	-0.0 (0.6)	-0.2 (0.7)	-0.1 (0.4)	0.2 (0.7)
cylinderGDR-ball	-1.2 (2.6)	-0.2 (1.1)	-0.3 (10.0)	-6.3 (65.2)	0.4 (12.7)	6.4 (65.2)
cylinderBDA-ball	-0.2 (0.9)	0.2 (0.8)	-0.5 (4.2)	5.0 (27.0)	-0.5 (2.4)	-5.0 (27.0)
cylinder-pancake	-0.1 (1.0)	0.2 (0.6)	0.2 (1.0)	-0.5 (2.5)	-0.2 (0.6)	0.5 (2.5)
cylinderECS-pancake	-0.0 (0.6)	0.1 (0.4)	0.0 (0.6)	-0.3 (2.1)	-0.1 (0.4)	0.3 (2.1)
cylinderGDR-pancake	-0.3 (1.6)	0.1 (0.6)	0.4 (1.6)	-0.4 (2.3)	-0.1 (0.6)	0.4 (2.3)
cylinderBDA-pancake	-0.1 (0.9)	0.2 (0.6)	-0.6 (4.7)	1.8 (23.1)	-0.5 (2.8)	-1.8 (23.1)

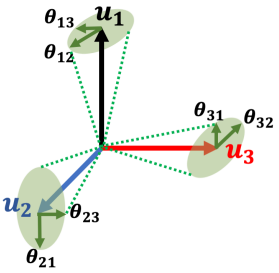

Fig. 4. Coupled Angles Demonstration. Given the reference orthonormal basis of eigenvectors u_1, u_2, and u_3, the angular variability of estimated eigenvector v_i about u_i can be measured in terms of six coupled angles θ_{ij}, i.e. the clockwise rotation from u_i to v_i projected on $u_i - u_j$ plane.

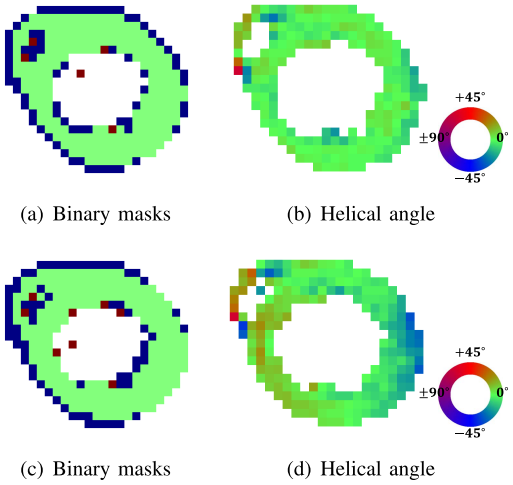

(a) Binary masks (b) Helical angle

(c) Binary masks (d) Helical angle

Fig. 5. SRI-MRI registration for one sample heart. The top row shows results for the optimum rigid space warp and the bottom row shows the same warp but with 70 μm translation along the *x*-axis. (a,c) The region with perfect overlay between MRI and SRI is coded with the green colour. The red and blue regions shows the mismatched regions between two masks. The Dice similarity metric is 0.84 for both experiments. (b, d) Variation in helical angle between DW-MRI and SRI scans are reported. Tensor fields, unlike binary masks, are sensitive to small changes in the warping transform.

bias in estimation of the orientations and the standard deviations represent the dispersion error, i.e. the radii of green ovals in Fig. 4.

3) Biophysical Parameters: Table II shows the average intracellular volume fraction v_{IC}, cardiomyocyte radius r, average dispersion in the sheetlet plane $\alpha_2 = \arctan(1/\kappa_2)$ and sheetlet-normal plane $\alpha_3 = \arctan(1/\kappa_3)$, and diffusivity along the cardiomyocyte direction in the intracellular ($d_{IC}^{\parallel}$) and extracellular ($d_{EC}^{\parallel}$) space. To avoid partial volume effects, values were reported on the left mid-ventricular wall.

4) Effects of Vascular Component: To investigate the impact of large vessels on estimated biophysical parameters, DW-MRI voxels were grouped in two groups based on the estimated volume fraction of vessels in the corresponding SRI voxels. Group one comprises voxels with less than 1% vascular component, whereas group two comprises voxels with over 5% vascular component. Table III compares the cardiomyocyte radius r and the fractional anisotropy (FA) in the extracellular compartment between two groups. No statistical difference was observed between two groups for the cell radius confirming that grouping the interstitial space and vascular components does not affect the biophysical parameter estimation. However, estimated FA for the extracellular compartment was found to be significantly lower for the second group (p-val$<$0.001). This finding is consistent with our expectation of almost free diffusion in large vessels.

B. Diffusion MRI Acquisition Scheme

To investigate the effectiveness of different diffusion acquisition schemes [12], [19] for estimation of biophysical parameters, we used (i) multi-shell diffusion data at a single diffusion time similar to [19], and (ii) fixed b-value and multi-diffusion-time data similar to [12]. The effect of acquisition schemes on estimation of cardiomyocyte radius and intracellular volume fraction are reported in Table IV and Table V, respectively. Multi-shell data acquisition was essential to observe the non-mono-exponential signal decay and estimate the intracellular volume fraction accurately (Table IV). Acquir-

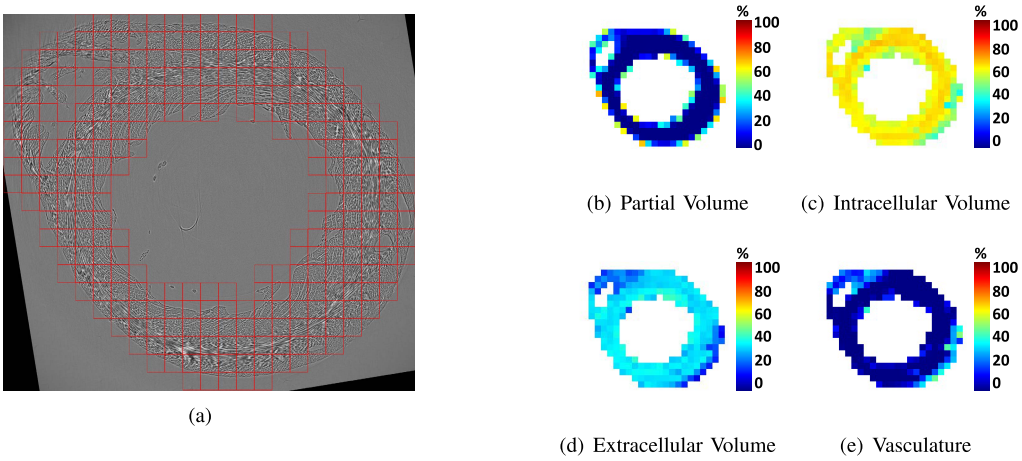

(a) (b) Partial Volume (c) Intracellular Volume (d) Extracellular Volume (e) Vasculature

Fig. 6. Estimated volume fractions for vessels, intra- and extracellular space from registered SRI scans. (a) One cross-section of the heart in short-axis orientation using high-resolution SRI data. The overlaid red squares represent DW-MRI voxels. Due to the heart curvature and limited MRI voxel size, the average of SRI binary masks within each red square is less than one at the myocardium boundaries. This effect is referred to as partial volume effect and is shown in panel b. Volume fractions for the intra- and extracellular space, and vessels excluding the partial volume effect are shown in panels (c), (d), and (e), respectively. Note that one quadrant of the heart was selected for manual annotation due to extensive manual labour required. Large vessels are mostly observed near the epicardium. The interstitial gaps between sheetlets appear to be larger near the subendocardium leading to a lower intracellular volume fraction.

ing data with multi-diffusion-time was essential for accurate estimation of cardiomyocyte radius (Table V).

C. SRI Microstructure Estimation

1) Registration: To compute structure tensors, parameters for quadrature filters were set as follows: centre frequency $f_0 = \pi/3$, bandwidth $B = 2$ octave, and spatial filter size $\omega = 11$. Fig. 5(a) shows the overlay of SRI binary mask on the DW-MRI binary mask following the image registration. Fig. 5(b) shows the variation in helix angles on the same slice. Figs. 5(c) and 5(d) demonstrate the effects of small changes in the warping transform on the maps; translating the SRI image by 70 µm along the x-axis, i.e. less than a voxel in the DW-MRI frame, does not change the overlap between the two binary masks (Dice metric = 0.84) but imposes a distinct bias in estimation of the helix angle.

2) Segmentation: Fig. 1 shows segmentation results in xy, xz, and yz planes for three slices within one DW-MRI voxel. Fig. 6 shows maps for partial volume effect, and volume fractions for cardiomyocytes, extracellular space and vessels based on manual segmentation in one slab corresponding to a quadrature of a DW-MRI slice.

3) Comparison Between SRI and DW-MRI: Cardiomyocyte and sheetlet orientation were quantified by averaging structure tensors in the corresponding DW-MRI voxels. Excellent agreement was observed between the diffusion eigenvectors $\boldsymbol{v}_1$, $\boldsymbol{v}_2$, and $\boldsymbol{v}_3$ and the structure tensor eigenvectors $\boldsymbol{u}_3$, $\boldsymbol{u}_2$, $\boldsymbol{u}_1$, respectively. The average (STD) of coupled angles about SRI eigenvectors in degree were 0.5(9.4), −0.5(4.8), −0.7(9.8), 2.3(15.9), 0.8(5.6), and −2.3(15.7) for θ_{12}, θ_{13}, θ_{21}, θ_{23}, θ_{31}, and θ_{32}, respectively. Computing the coupled angles between compartment models and SRI yielded similar results to Table. I and are not shown here.

Fig. 7 shows Bland-Altman plots to compare intracellular volume fractions estimated from the SRI scans against the figures measured by each of the compartment models. The Bland-Altman plots showed a small bias of 1.5% for the cylinderGDR-pancake model and a moderate bias of 7.1%, 7.8%, and 6.7% for the cylinder-pancake, cylinderECS-pancake, and cylinderBDA-pancake models, respectively. However, the non-zero slope observed in the Bland-Altman plots suggests a systematic difference for estimation of the intracellular volume fraction. For the cylinder-pancake and the cylinderBDA-pancake models, the slope is modest for intracellular volume fractions between 58-65%.

IV. Discussion

Ten different compartment models were developed, studied, and compared to derive microstructural tissue parameters in the heart. This study included three models previously proposed by Hsu *et al.* [19], Kim *et al.* [12], and McClymont *et al.* [23]. The tensor-tensor model [19] improved the RMSE by ≈ 28% compared to DTI but failed to account for restricted diffusion in cardiomyocytes. The tensor-tensor model also underestimated the intracellular volume fraction. This finding is consistent with results reported in [19]. The cylinder-ball [12] modelled the restricted diffusion and provided reasonable estimates for cardiomyocytes radius but fit the data poorly; the RMSE was ≈ 92% higher compared to DTI. The model proposed by Kim *et. al.* [12] addressed both issues but the estimated radius of 30 µm along the secondary diffusion eigenvector was almost twice the physical sizes known from the literature [20]. We show that previous models do not fit well to the measured signals, or yield unrealistic biophysical parameters (Table II)

Seven new two-compartment models with combination of extended cylinder models and diffusion tensors were investigated. Among the proposed models, the cylinderECS-ball, cylinderBDA-ball, and cylinderGDR-ball had higher RMSE compared to DTI. This poor fitting performance can be

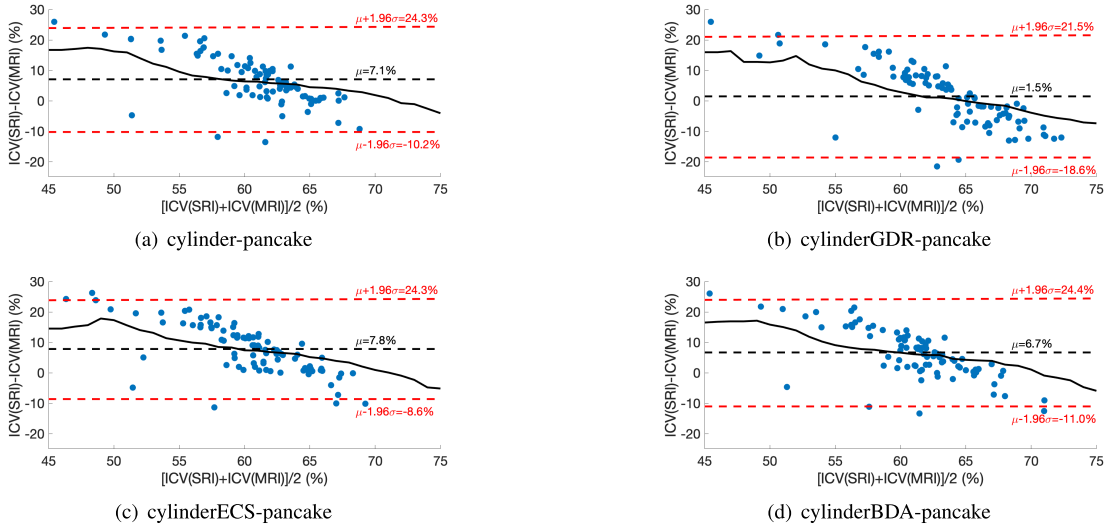

(a) cylinder-pancake (b) cylinderGDR-pancake

(c) cylinderECS-pancake (d) cylinderBDA-pancake

Fig. 7. Bland-Altman plots for comparison between SRI and DW-MRI intracellular volume fractions. The result is based on the ROI shown in Fig. 6(a) on a mid-ventricular wall to avoid partial volume effect with the surrounding gel/buffer. The solid black line represents the local average of the scattered points using a rectangular moving average window of size 15. The dashed red lines represent the 95% confidence interval, i.e. the mean±1.96SD. The dashed black line represents the overall bias.

TABLE II
ESTIMATED BIOPHYSICAL PARAMETERS ON A SLICE FROM LEFT VENTRICLE WALL (FIRST HEART)*. [MEAN(STD)]

	AIC[$\times 10^3$]	RMSE	v_{IC}[%]	r [μm]	r_s [μm]	r_l [μm]	d_{IC} [μm^2/ms]	d_{EC} [μm^2/ms]	α_2 [degree]	α_3 [degree]
Reference values [20], [21]	—	—	65.0 (3.6)	9.5 (0.5)	6.0 (0.7)	15.3 (1.0)	—	—	—	—
SRI	—	—	63.9 (4.4)	6.4 (1.1)	5.3 (1.5)	7.9 (0.8)	—	—	—	—
tensor	-1.36 (0.04)	0.025 (0.002)	—	—	—	—	—	—	—	—
tensor-tensor [19]	**-1.54 (0.11)**	**0.018 (0.003)**	54.5 (5.2)	—	—	—	0.84 (0.04)	2.01 (0.02)	—	—
cylinder-ball [12]	-0.97 (0.14)	0.048 (0.011)	70.2 (6.1)	7.2 (0.9)	—	—	0.91 (0.04)	2.00 (0.00)	—	—
cylinderECS-ball-stick [23]	-1.51 (0.09)	0.019 (0.003)	68.1 (6.4)	—	7.5 (2.5)	33.6 (8.3)	0.89 (0.06)	2.14 (0.20)	—	—
cylinderECS-ball	-1.29 (0.04)	0.027 (0.002)	69.7 (6.5)	—	4.6 (1.1)	10.6 (1.4)	0.94 (0.05)	2.01 (0.02)	—	—
cylinderGDR-ball	-1.06 (0.17)	0.042 (0.011)	81.4 (8.2)	13.2 (0.8)	—	—	1.03 (0.06)	2.02 (0.11)	—	—
cylinderBDA-ball	-1.25 (0.10)	0.030 (0.006)	71.0 (8.2)	4.1 (1.4)	—	—	1.84 (0.42)	2.08 (0.16)	32.2 (11.6)	4.0 (4.3)
cylinder-pancake	-1.40 (0.06)	0.023 (0.002)	58.0 (6.6)	7.8 (0.9)	—	—	0.79 (0.05)	2.02 (0.07)	—	—
cylinderECS-pancake	-1.42 (0.06)	0.022 (0.002)	56.9 (7.2)	—	**5.6 (1.9)**	**7.9 (0.9)**	0.81 (0.04)	2.02 (0.09)	—	—
cylinderGDR-pancake	-1.52 (0.08)	0.019 (0.003)	**64.0 (8.5)**	12.6 (2.1)	—	—	0.88 (0.06)	2.09 (0.24)	—	—
cylinderBDA-pancake	-1.40 (0.06)	0.023 (0.002)	58.2 (6.7)	**6.8 (1.9)**	—	—	0.99 (0.38)	2.02 (0.04)	6.1 (10.7)	2.9 (5.6)

* Mean and STD of parameters are reported on a single DW-MRI slice shown in Fig. 6. To avoid partial volume effect, averaging is performed over voxels in the mid-ventricle wall only. Findings were consistent between two hearts. See supplementary Table I for results on the second heart.
** Bold figures on each column represent the best performing biophysical model in this study.

explained with the inability of these models to represent the anisotropy along the second and the third diffusion eigenvectors, whereby both the standard cylinder model and the ball are fully isotropic about the primary diffusion eigenvector. Using a pancake to represent the extracellular space addressed this issue by allowing a different diffusivity along the sheetlet-normal direction (Table II).

Supplementary Figure 3 demonstrated the RMSE distribution in one cross-section cut in the short-axis view for the four cylinder-pancake models. All four models reduced the RMSE comparing to DTI. Unlike DTI, these models were also an unbiased estimator of the measured DW-MR signals as confirmed by Bland-Altman plots in supplementary Figure 4. Employing a more complex biophysical model may result in a reduced RMSE but note that the estimated RMSE could be also attributed to low SNR during DW-MRI acquisition; RMSE cannot be reduced below the noise power unless the model is over-fitted to noise rather than data. The three-compartment model [23] studied here did not improve the RMSE beyond the proposed two-compartment models (Table II). This observation may suggest that the inherent noise could be the main reason for the modest fitting performance in this study. While improving data fitting could be a challenge as biophysical models provide a simplified

TABLE III
COMPARE THE CARDIOMYOCYTE RADIUS AND THE EXTRACELLULAR FA BETWEEN TWO GROUPS OF VOXELS WITH DIFFERENT VOLUME FRACTIONS OF VESSELS USING T-TEST

parameter	$v_{\text{vessels}} < 1\%$ $(n = 18)$	$v_{\text{vessels}} > 5\%$ $(n = 12)$	p-value
r [μm]	7.3 ± 1.9	7.9 ± 2.2	0.45
FA	0.61 ± 0.078	0.48 ± 0.11	$< 0.001^*$

TABLE IV
DEPENDENCE OF BIOPHYSICAL PARAMETERS ON B-VALUE. PARAMETERS ARE REPORTED FOR CYLINDER-PANCAKE MODEL USING ALL FIVE DIFFUSION TIMES AND A SINGLE B-VALUE

b[s/mm^2]	RMSE	v_{IC}[%]	r[μm]	d_{IC}[μm^2/ms]	d_{EC}[μm^2/ms]
270	0.0120	62.1	3.2	0.80	2.28
620	0.0129	55.2	3.5	0.79	2.06
1100	0.0133	46.5	3.1	0.72	2.01
1730	0.0148	39.1	3.1	0.66	2.02
2490	0.0159	33.8	3.6	0.60	2.01
All b-values	0.0244	59.3	6.8	0.79	2.04

TABLE V
DEPENDENCE OF BIOPHYSICAL PARAMETERS ON DIFFUSION TIME. PARAMETERS ARE REPORTED FOR CYLINDER-PANCAKE MODEL USING ALL B-VALUES AND A SINGLE DIFFUSION TIME

DT[ms]	RMSE	v_{IC}[%]	r[μm]	d_{IC}[μm^2/ms]	d_{EC}[μm^2/ms]
10	0.0152	65.6	4.9	0.95	2.00
20	0.0145	67.1	6.3	0.94	2.01
30	0.0158	66.3	7.2	0.91	2.03
40	0.0167	65.7	7.8	0.90	2.01
50	0.0192	65.6	8.5	0.87	2.04
All DT	0.0244	59.3	6.8	0.79	2.04

sketch of the underlying microstructure, their adequacy should be also assessed on how well the biophysical parameters are represented. An acceptable biophysical model should not only fit the data sufficiently well, but also provide a reasonable estimation of the underlying tissue microstructure [14].

Three specific microstructure properties including cardiomyocyte radius, the intracellular volume fraction, and cardiomyocyte dispersion were examined. Among the four proposed models with improved fitting performance (bottom four rows in Table II), the cylinderBDA-pancake model yielded the closest approximation for the cardiomyocyte radius (Table II). The cylinderECS-pancake model also provided good approximations for the small and large radii assuming an elliptical cross-section for cardiomyocytes. However, the cylinderGDR-pancake model significantly overestimated the cardiomyocyte radius with respect to the SRI measurements. The closest estimation to the reference value for the intracellular volume fraction [21] was provided by the cylinderGDR-pancake (64%) whereas the remaining three models yielded slightly lower approximations ($\approx 60\%$). However, observing the residuals on a voxel-based comparison suggested that the estimation error for ICV depends on its true value (Fig. 7). This dependence is modest when ICV is around $\approx 62\%$ and more distinct when ICV is at the other extremes. One potential reason for this observation is that the extracellular space is modelled with a planar/oblate tensor (pancake) representing the cleavage planes between sheetlets in these models. The interstitial space between cardiomyocytes in sheetlets is not explicitly modelled here. Therefore, in voxels with tightly packed sheetlets, ICV is overestimated and in voxels with large gaps between sheetlets or large vessels, ICV is underestimated. Of note, the cylinderBDA-pancake is the only model that parameterises dispersion.

To facilitate parameter estimation for biophysical models, multi-diffusion-time, multi-shell, and multi-direction data are needed. Here we showed that previous acquisitions schemes that only acquired a single shell with different diffusion times [12] are inadequate as the intracellular volume fraction varies strongly with b-value (Table IV). Acquiring multiple shell but with a single diffusion time [19] is also insufficient as the cell radius r varies strongly with the diffusion time (Table V). Here a diffusion scheme with five different diffusion times and six different gradient strengths was used.

One specific challenge to develop and refine biophysical models is access to ground-truth parameters at the cellular level [14], [22]. Here, SRI was employed as a solution for two reasons: first, it provides information on the 3D tissue microstructure at a high spatial resolution suitable for virtual histology. Second, the prepared tissue samples can be imaged immediately following the MRI acquisitions without further sample preparation. Here intracellular volume fractions for intracellular, extracellular, and vessels were quantitated using a semi-automatic segmentation technique (Fig. 6). The average ICV estimated from the reconstructed SRI scans was 63.9%. Our finding was consistent with results reported in [21]. Here, eight individual cardiomyocytes were manually segmented and the mean and SD for their radius were reported in Table II. The estimated radius from reconstructed SRI scans was 30% lower than the value reported in [20]. This variation could be attributed to anatomical variation between species [38].

While our work represents a significant advancement over previously published work, our study had the following limitations. Firstly, simplified two-compartment models were considered in this study with limited ability to account for the capillary network and partial volume effects. In this study, the interstitial space between cardiomyocytes and vascular components were combined into one effective compartment similar to Hsu *et al.* [19] and Kim *et al.* [12]. Given the maximum diffusion time of 50 ms and the buffer mean diffusivity of $2.0\mu\text{m}^2/\text{ms}$, the average diffusion distance would be $\approx \sqrt{2Dt} = 14\,\mu\text{m}$. This distance is three times lower than the average diameter of $\approx 50\,\mu\text{m}$ for large vessels estimated from SRI scans. Therefore, we postulate that the restriction effects imposed by vessels boundaries would be negligible as confirmed in Table III. However, more complex multi-compartment models may be warranted.

Secondly, this study focuses on healthy control hearts, and the sensitivity of estimated biophysical parameters to disease is subject of future work. Thirdly, the manual segmentation of SRI data was highly laborious, limiting its application. In future, advanced deep networks could help with automatic segmentation of SRI data for extracting additional structural properties including cell size and dispersion. Fourthly, two healthy mouse hearts were used in this study. Despite the limited number of hearts, note that each heart is comprised of a few hundreds of voxels with a diverse range of structural properties over which the estimated biophysical parameters were validated.

To improve SNR, this study employed different echo times for each diffusion time. This strategy has the effect of producing different T2 weighting for data acquired at different diffusion times. To address this effect, the data was normalised with respect to b0 signal collected for each diffusion time. However, if the tissue has compartments with different T2 values, the relative contributions of the compartments to the signal will not be the same at all diffusion times due to the difference in the amount of T2 decay. Kim *et al.* [12] investigated this effect on a cylinder-ball model and reported minor effects on estimated biophysical parameters. Here, we followed a similar approach to Kim *et al.* [12].

Water exchange between the intra- and extracellular compartments may also influence our measurements. Here, impermeable cylinders were employed to represent cardiomyocytes assuming zero water exchange between compartments. Forder *et al.* [39] simulated the influence of water exchange on measurements using a simple tissue model [40] with a diffusion time of 11 ms and concluded that the difference between exchange rates of 0 and the estimated upper limit of 27 Hz [41] is negligible. However, we recognise that permeability is of potential importance, and this is subject of future investigation.

The employed *ex vivo* preservation and fixation technique may affect the estimated biophysical properties. Fixatives like formaldehyde stabilise microstructural organisation within tissues and make them metabolically inactive [42]. However, these fixatives alter the chemical and physical environments contributing to the DW-MR signals [42]. Washing the excess fixative from samples via immersion in PBS could help to reduce these effects [42]. Agger *et al.* [43] compared perfusion versus immersion fixation and concluded that the latter should be preferred as this method provided diffusion data closest to fresh hearts. However, perfusion fixation with formalin yielded the best tractography results [43]. The effects of continuous formalin fixation on diffusion tensor properties were studied by Lohr *et al.* [44]; mean diffusivity and FA were reduced by 22% and 10% post-fixation after 7 days [44].

This study presented new developments in DW-MRI biophysical modelling of myocardial microstructure based on preclinical *ex vivo* data. Translation to clinical applications with *in vivo* imaging would bring new challenges: firstly, access to multiple diffusion times and very high b-values is limited on clinical scanners. Secondly, blood flow in the vascular network may have a significant effect on the apparent diffusion coefficient. Thirdly, heart motion should be compensated properly for enhanced sensitivity to water molecules diffusion.

This study investigated the feasibility of DW-MRI biophysical models in heart. However, signal representation techniques have advantages too and may be more sensitive in distinguishing healthy tissue versus disease. If a model is not close to reality due to oversimplification of the tissue architecture, the model parameters may not be useful. While changes of values in signal representations are never *wrong*, this variation may not be attributed to specific tissue properties easily; biophysical models would allow for direct measurements of specific tissue properties.

V. Conclusion

We proposed seven new two-compartment models of DW-MRI to quantitate tissue microstructure in heart. Our results suggested an oblate/planar diffusion anisotropy in the extracellular space due to interstitial gaps between sheetlets. Four extended version of cylinder models were studied here to represent the intracellular space. The cylinderBDA-pancake model represented anatomical findings closest as it also allows for modelling dispersion. The cylinderBDA-pancake yielded volume fraction = 58% and radius = 6.8 μm in agreement with prior literature and SRI data analysis. Our results suggested that multi-diffusion-time multi-shell multi-direction diffusion schemes are required for a reliable estimation of biophysical parameters.

Appendix A
Signal Model for a Cylinder

The signal model for a cylinder is represented by product of signals parallel and perpendicular to the cylinder axis $\hat{\boldsymbol{n}}$ [25], [45], [46],

$$S_{\text{cyl}}(\hat{\boldsymbol{n}}, d_{\parallel}, r) = s_0 \exp -L_{\parallel}(d_{\parallel}) \left[\boldsymbol{g}^T \hat{\boldsymbol{n}}\right]^2 \times \exp -L_{\perp}(r, d_{\parallel}) \left[\boldsymbol{g}^T \boldsymbol{g} - \left[\boldsymbol{g}^T \hat{\boldsymbol{n}}\right]^2\right], \quad (21)$$

where $d_{\parallel}$ is the diffusivity along the cylinder axis $\hat{\boldsymbol{n}}$ and r is the cylinder radius.

Assuming non-restricted diffusion along the parallel direction and Gaussian Phase Distribution (GPD) approximation in the perpendicular direction, $L_{\parallel}$ and $L\ \perp$ are defined as follows [45]:

$$L_{\parallel}(d_{\parallel}) = \gamma^2 \delta^2 (\Delta - \delta/3) d_{\parallel}, \quad (22)$$

$$\begin{aligned} L_{\perp}(d_{\parallel}, r) = 2\gamma^2 \sum_{m=1}^{\infty} \Big[d_{\parallel}^2 \beta_m^6 (r^2 \beta_m^2 - 1)\Big]^{-1} \\ \ldots \Big[2 d_{\parallel} \beta_m^2 \delta - 2 \\ + \ldots \ 2\exp[-d_{\parallel} \beta_m^2 \delta] \\ + \ldots \ 2\exp[-d_{\parallel} \beta_m^2 \Delta] \\ - \ldots \ \exp[-d_{\parallel} \beta_m^2 (\Delta - \delta)] \\ - \ldots \ \exp[-d_{\parallel} \beta_m^2 (\Delta + \delta)]\Big]. \end{aligned} \quad (23)$$

Here, β_m is the m^{th} root of equation $J_1'(\beta_m r) = 0$ and J_1' is the derivative of the Bessel function of the first kind, order one.

References

[1] S. Nielles-Vallespin, A. Scott, P. Ferreira, Z. Khalique, D. Pennell, and D. Firmin, "Cardiac diffusion: Technique and practical applications," *J. Magn. Reson. Imag.*, vol. 52, no. 2, pp. 348–368, Aug. 2020.

[2] A. Kanai and G. Salama, "Optical mapping reveals that repolarization spreads anisotropically and is guided by fiber orientation in guinea pig hearts," *Circulat. Res.*, vol. 77, no. 4, pp. 784–802, Oct. 1995.

[3] I. Teh *et al.*, "Mapping cardiac microstructure of rabbit heart in different mechanical states by high resolution diffusion tensor imaging: A proof-of-principle study," *Prog. Biophys. Mol. Biol.*, vol. 121, no. 2, pp. 85–96, Jul. 2016.

[4] M. A. Konstam, D. G. Kramer, A. R. Patel, M. S. Maron, and J. E. Udelson, "Left ventricular remodeling in heart failure: Current concepts in clinical significance and assessment," *JACC, Cardiovascular Imag.*, vol. 4, no. 1, pp. 98–108, 2011.

[5] S. A. Wickline, E. D. Verdonk, A. K. Wong, R. K. Shepard, and J. G. Miller, "Structural remodeling of human myocardial tissue after infarction. Quantification with ultrasonic backscatter," *Circulation*, vol. 85, no. 1, pp. 259–268, Jan. 1992.

[6] D. McClymont *et al.*, "Evaluation of non-Gaussian diffusion in cardiac MRI," *Magn. Reson. Med.*, vol. 78, no. 3, pp. 1174–1186, Sep. 2017.

[7] T. G. Reese, R. M. Weisskoff, R. N. Smith, B. R. Rosen, R. E. Dinsmore, and V. J. Wedeen, "Imaging myocardial fiber architecture *in vivo* with magnetic resonance," *Magn. Reson. Med.*, vol. 34, no. 6, pp. 786–791, Dec. 1995.

[8] J. Chen *et al.*, "Regional ventricular wall thickening reflects changes in cardiac fiber and sheet structure during contraction: Quantification with diffusion tensor MRI," *Amer. J. Physiol.-Heart Circulatory Physiol.*, vol. 289, no. 5, pp. H1898–H1907, Nov. 2005.

[9] D. A. Yablonskiy and A. L. Sukstanskii, "Theoretical models of the diffusion weighted MR signal," *NMR Biomed.*, vol. 23, no. 7, pp. 661–681, Jun. 2010.

[10] I. O. Jelescu and M. D. Budde, "Design and validation of diffusion MRI models of white matter," *Frontiers Phys.*, vol. 5, p. 61, Nov. 2017.

[11] H. Lombaert *et al.*, "Human atlas of the cardiac fiber architecture: Study on a healthy population," *IEEE Trans. Med. Imag.*, vol. 31, no. 7, pp. 1436–1447, Jul. 2012.

[12] S. Kim, G. Chi-Fishman, A. S. Barnett, and C. Pierpaoli, "Dependence on diffusion time of apparent diffusion tensor of *ex vivo* calf tongue and heart," *Magn. Reson. Med.*, vol. 54, no. 6, pp. 1387–1396, 2005.

[13] C. Bingham, "An antipodally symmetric distribution on the sphere," *Ann. Statist.*, vol. 2, no. 6, pp. 1201–1225, 1974.

[14] D. S. Novikov, V. G. Kiselev, and S. N. Jespersen, "On modeling," *Magn. Reson. Med.*, vol. 79, no. 6, pp. 3172–3193, 2018.

[15] V. J. Wedeen, P. Hagmann, W.-Y. I. Tseng, T. G. Reese, and R. M. Weisskoff, "Mapping complex tissue architecture with diffusion spectrum magnetic resonance imaging," *Magn. Reson. Med.*, vol. 54, no. 6, pp. 1377–1386, 2005.

[16] M. Lohezic *et al.*, "Interrogation of living myocardium in multiple static deformation states with diffusion tensor and diffusion spectrum imaging," *Prog. Biophys. Mol. Biol.*, vol. 115, nos. 2–3, pp. 213–225, Aug. 2014.

[17] Y. Assaf, T. Blumenfeld-Katzir, Y. Yovel, and P. J. Basser, "AxCaliber: A method for measuring axon diameter distribution from diffusion MRI," *Magn. Reson. Med.*, vol. 59, no. 6, pp. 1347–1354, Jun. 2008.

[18] H. Zhang, T. Schneider, C. A. Wheeler-Kingshott, and D. C. Alexander, "NODDI: Practical *in vivo* neurite orientation dispersion and density imaging of the human brain," *NeuroImage*, vol. 61, no. 4, pp. 1000–1016, Jul. 2012.

[19] E. W. Hsu, D. L. Buckley, J. D. Bui, S. J. Blackband, and J. R. Forder, "Two-component diffusion tensor MRI of isolated perfused hearts," *Magn. Reson. Med.*, vol. 45, no. 6, pp. 1039–1045, 2001.

[20] Y.-F. Chen, S. Said, S. E. Campbell, and A. M. Gerdes, "A method to collect isolated myocytes and whole tissue from the same heart," *Amer. J. Physiol.-Heart Circulatory Physiol.*, vol. 293, no. 3, pp. H2004–H2006, Sep. 2007.

[21] J. Greiner, A. C. Sankarankutty, G. Seemann, T. Seidel, and F. B. Sachse, "Confocal microscopy-based estimation of parameters for computational modeling of electrical conduction in the normal and infarcted heart," *Frontiers Physiol.*, vol. 9, p. 239, Apr. 2018.

[22] I. O. Jelescu, M. Palombo, F. Bagnato, and K. G. Schilling, "Challenges for biophysical modeling of microstructure," *J. Neurosci. Methods*, vol. 344, Oct. 2020, Art. no. 108861.

[23] D. McClymont, I. Teh, H. Whittington, C. A. Lygate, and J. E. Schneider, "Inferring cell morphology in the heart with a compartment model of diffusion mri," in *Proc. Int. Soc. Magn. Reson. Med.*, 2017, p. 1743.

[24] I. Teh *et al.*, "Validation of diffusion tensor MRI measurements of cardiac microstructure with structure tensor synchrotron radiation imaging," *J. Cardiovascular Magn. Reson.*, vol. 19, no. 1, pp. 1–14, Dec. 2017.

[25] E. Panagiotaki, T. Schneider, B. Siow, M. G. Hall, M. F. Lythgoe, and D. C. Alexander, "Compartment models of the diffusion mr signal in brain white matter: A taxonomy and comparison," *NeuroImage*, vol. 59, no. 3, pp. 2241–2254, 2012.

[26] M. Tariq, T. Schneider, D. C. Alexander, C. A. G. Wheeler-Kingshott, and H. Zhang, "Bingham–NODDI: Mapping anisotropic orientation dispersion of neurites using diffusion MRI," *NeuroImage*, vol. 133, pp. 207–223, Jun. 2016.

[27] S. N. Sotiropoulos, T. E. J. Behrens, and S. Jbabdi, "Ball and rackets: Inferring fiber fanning from diffusion-weighted MRI," *NeuroImage*, vol. 60, no. 2, pp. 1412–1425, Apr. 2012.

[28] I. Teh *et al.*, "Resolving fine cardiac structures in rats with high-resolution diffusion tensor imaging," *Sci. Rep.*, vol. 6, no. 1, p. 30573, Aug. 2016.

[29] N. T. Vo, M. Drakopoulos, R. C. Atwood, and C. Reinhard, "Reliable method for calculating the center of rotation in parallel-beam tomography," *Opt. Exp.*, vol. 22, no. 16, pp. 19078–19086, 2014.

[30] C. Raven, "Numerical removal of ring artifacts in microtomography," *Rev. Sci. Instrum.*, vol. 69, no. 8, pp. 2978–2980, Aug. 1998.

[31] F. P. Vidal, J. M. Létang, G. Peix, and P. Cloetens, "Investigation of artefact sources in synchrotron microtomography via virtual X-ray imaging," *Nucl. Instrum. Methods Phys. Res. B, Beam Interact. Mater. At.*, vol. 234, no. 3, pp. 333–348, Jun. 2005.

[32] A. C. Kak and M. Slaney, *Principles of Computerized Tomographic Imaging*. New York, NY, USA: IEEE Press, 1987.

[33] G. H. Granlund and H. Knutsson, *Signal Processing for Computer Vision*. Dordrecht, The Netherlands: Springer, 1995.

[34] H. Knutsson, "Representing local structure using tensors," in *Proc. 6th Scandin. Conf. Image Anal. (SCIA)*. Oulu, Finland: Linköping Univ. Electronic Press, 1989, pp. 244–251.

[35] D. Forsberg. (2020). *Tensor Processing*. https://www.github.com/fordanic/tensor-processing

[36] P. A. Yushkevich *et al.*, "User-guided 3D active contour segmentation of anatomical structures: Significantly improved efficiency and reliability," *NeuroImage*, vol. 31, no. 3, pp. 1116–1128, Jul. 2006.

[37] C. Rau, U. Wagner, Z. Pešić, and A. De Fanis, "Coherent imaging at the diamond beamline I13," *Phys. Status Solidi A*, vol. 208, no. 11, pp. 2522–2525, Nov. 2011.

[38] H. Satoh, L. M. Delbridge, L. A. Blatter, and D. M. Bers, "Surface:Volume relationship in cardiac myocytes studied with confocal microscopy and membrane capacitance measurements: Species-dependence and developmental effects," *Biophysical J.*, vol. 70, no. 3, pp. 1494–1504, Mar. 1996.

[39] J. R. Forder, J. D. Bui, D. L. Buckley, and S. J. Blackband, "MR imaging measurement of compartmental water diffusion in perfused heart slices," *Amer. J. Physiol.-Heart Circulatory Physiol.*, vol. 281, no. 3, pp. H1280–H1285, Sep. 2001.

[40] G. J. Stanisz, J. G. Li, G. A. Wright, and R. M. Henkelman, "Water dynamics in human blood via combined measurements of T_2 relaxation and diffusion in the presence of gadolinium," *Magn. Reson. Med.*, vol. 39, no. 2, pp. 223–233, Feb. 1998.

[41] K. M. Donahue, D. Burstein, W. J. Manning, and M. L. Gray, "Studies of Gd-DTPA relaxivity and proton exchange rates in tissue," *Magn. Reson. Med.*, vol. 32, no. 1, pp. 66–76, Jul. 1994.

[42] P. E. Thelwall, T. M. Shepherd, G. J. Stanisz, and S. J. Blackband, "Effects of temperature and aldehyde fixation on tissue water diffusion properties, studied in an erythrocyte ghost tissue model," *Magn. Reson. Med.*, vol. 56, no. 2, pp. 282–289, 2006.

[43] P. Agger, T. Lass, M. Smerup, J. Frandsen, and M. Pedersen, "Optimal preservation of porcine cardiac tissue prior to diffusion tensor magnetic resonance imaging," *J. Anatomy*, vol. 227, no. 5, pp. 695–701, Nov. 2015.

[44] D. Lohr, M. Terekhov, F. Veit, and L. M. Schreiber, "Longitudinal assessment of tissue properties and cardiac diffusion metrics of the *ex vivo* porcine heart at 7 T: Impact of continuous tissue fixation using formalin," *NMR Biomed.*, vol. 33, no. 7, p. e4298, Jul. 2020.

[45] P. Van Gelderen, D. DesPres, P. C. M. Vanzijl, and C. T. W. Moonen, "Evaluation of restricted diffusion in cylinders," *J. Magn. Reson.*, vol. 103, no. 3, pp. 255–260, 1994.

[46] H. Zhang, P. L. Hubbard, G. J. M. Parker, and D. C. Alexander, "Axon diameter mapping in the presence of orientation dispersion with diffusion MRI," *NeuroImage*, vol. 56, no. 3, pp. 1301–1315, Jun. 2011.